Tuning Histone Site Selectivity in the Nucleosome with Organometallic Agents

Andrea Levy[1], Zenita Adhireksan[2,3], Thibaud von Erlach[1], Giulia Palermo[1*], Alexey A. Nazarov[4], Christian G. Hartinger[5], Paul J. Dyson[4], Ursula Rothlisberger[1#] & Curtis A. Davey[2,3,6#]

[1] Laboratory of Computational Chemistry and Biochemistry, Ecole Polytechnique Fédérale de Lausanne, Lausanne CH-1015, Switzerland

[2] School of Biological Sciences, Nanyang Technological University, 60 Nanyang Drive, Singapore 637551

[3] NTU Institute of Structural Biology, Nanyang Technological University, 59 Nanyang Drive, Singapore 636921

[4] Institute of Chemical Sciences and Engineering, École Polytechnique Fédérale de Lausanne (EPFL), Lausanne, 1015 Switzerland

[5] School of Chemical Sciences, University of Auckland, Private Bag 92019, Auckland 1142, New Zealand

[6] Małopolska Centre of Biotechnology, Jagiellonian University, 31-007 Kraków, Poland

[*] Present address: Department of Bioengineering and Department of Chemistry, University of California Riverside, 900 University Avenue, Riverside, CA, 52512, USA

[#] Corresponding authors: U.R. (ursula.roethlisberger@epfl.ch), C.A.D. (curtis.davey@uj.edu.pl)

ABSTRACT

Histone alterations are increasingly recognized as oncogenic drivers, yet the chromatin drug portfolio is largely limited to DNA-targeting agents and inhibitors of chromatin-modifying proteins. Because nucleosomes play a foundational role in genomic regulation while presenting chemically diverse protein surfaces, principles of site discrimination could open up new possibilities for therapeutic interventions. Here, we show that ruthenium- and osmium-based compounds can be tuned to selectively bind specific histone sites in the nucleosome. The identity of the metal cation and non-leaving ligands dictates adduct stability and whether complexes target exposed electronegative patches or internal crevices, with steric accessibility, hydrophobic/van der Waals complementarity, and ligand lability governing site specificity. Our findings yield design rules for selective engagement of histones, suggesting that organometallic compounds can be rationally developed to target defined chromatin features and expand the scope of epigenetic therapeutics.

GRAPHICAL ABSTRACT

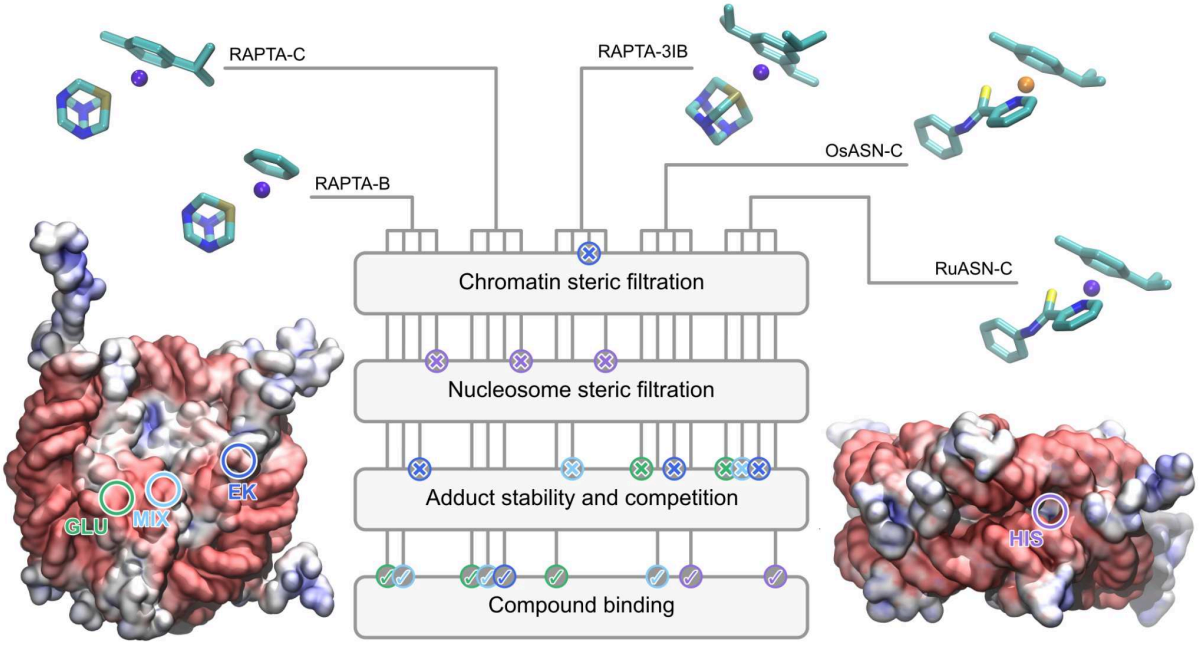

Histone mutations and aberrant histone isoform/variant expression levels have recently emerged as common oncogenic drivers, referred to as 'oncohistones'.[1–4] With histone dysregulation materializing as a signature shared by both cancerous and aged cells, these foundational proteins are emerging as multifunctional therapeutic targets.[5–7] Similar to how epigenetic drugs undermine cancer cell dependencies on specific chromatin-associated proteins, selective histone targeting could exploit cancer-specific vulnerabilities arising from disproportionate reliance on activity linked to a defined histone isoform or variant. Indeed, we had discovered a therapeutic (anticancer) potential in selectively targeting histone sites in chromatin for certain Ru- and Au-based compounds.[8–12]

Our body of work on the interaction of a variety of Pt-, Au-, Ru, and Os-based drugs/compounds with the nucleosome revealed that some agents preferentially bind histone proteins rather than DNA.[8–16] Among histone-binders, those based on the RAPTA [(η^6-p-arene)Ru(1,3,5-triaza-7-phosphaadamantane)Cl_2] anti-metastasis/tumor drugs commonly coordinate to glutamate sites in the nucleosome acidic patch,[8–12] while Ru/Os-arene agents with bidentate O,O- or S,N-ligands coordinate only to imidazole groups[16] (**Figures 1**, **S1** & **S2**). One of these histone binding sites (MIX site) lies in the acidic patch and is common to the coordination of both classes of compounds, as it is composed of both a glutamate and a histidine side chain and is capable of engaging in either monodentate or bidentate metal cation coordination (**Figures 1a–c**). Conversely, the other RAPTA-binding site (GLU site) in the acidic patch is composed of two glutamate side chains (**Figures 1a–c**) and is capable of bidentate metal cation coordination. In contrast, an internal motif (HIS site) consisting of a single histidine side chain is present in the nucleosome crevice (**Figures 1a** & **1d**). A fourth type of histone coordinating site (EK site), involving a carboxylate/amine motif, is unique to the binding of RAPTA-C (C=cymene; **Figures 1a** & **1e**). Details on data collection are reported in the Supporting Information (SI), **Tables S1–S3**.

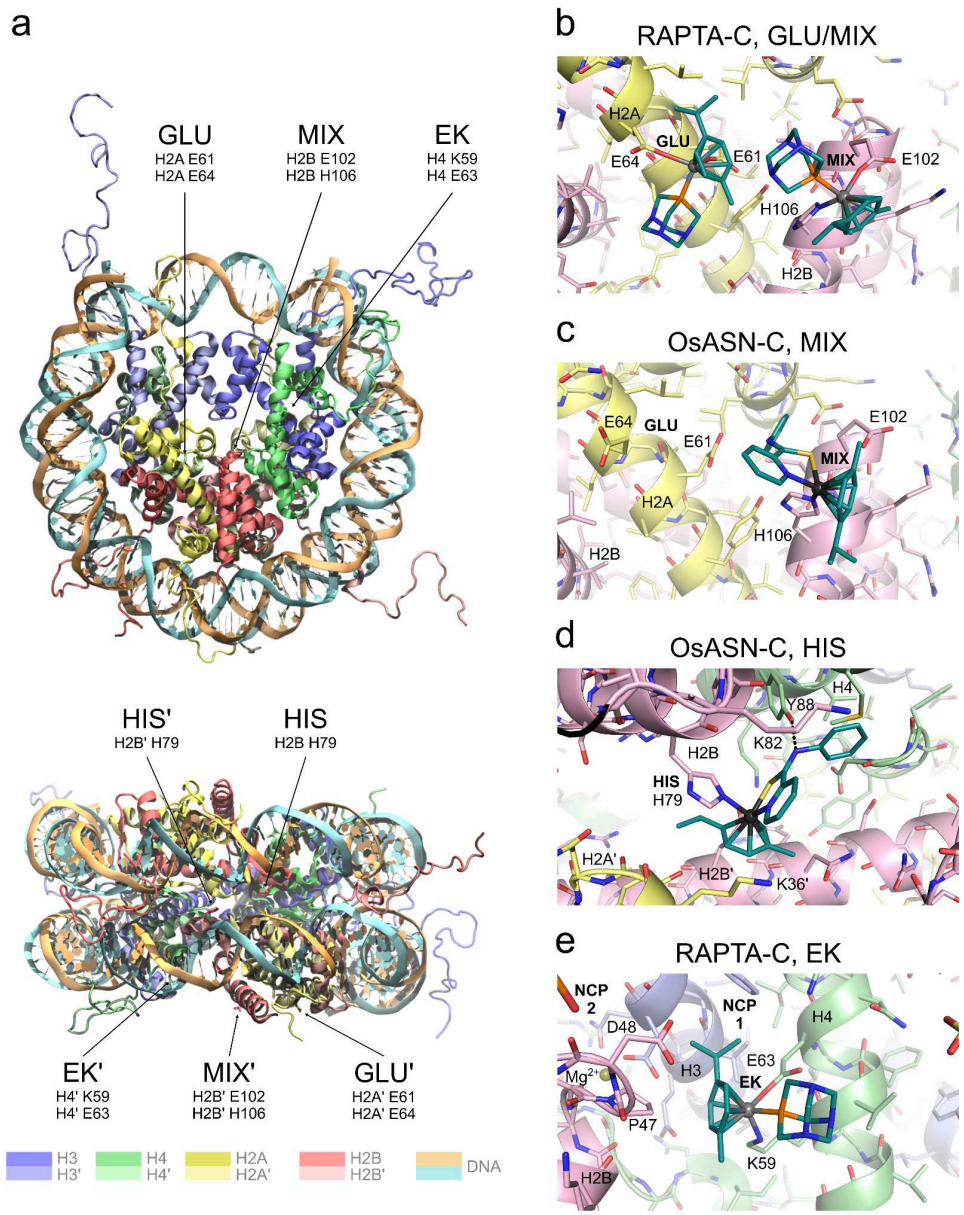

Figure 1. Nucleosome structure and organometallic compound-histone binding sites in the nucleosome. **a)** Nucleosome core particle (NCP; PDB ID 1KX5), highlighting the binding sites observed in crystal structures for Ru/Os compounds (´, 2-fold symmetry-related sites). **b–e)** NCP crystal structure-based details of RAPTA-C and OsASN-C (PDB ID 4J8U) binding at the four different types of coordinating histone sites. (in d, dashed line for hydrogen bond).

Given the intriguing nature of site selectivity between the different classes of Ru/Os compounds, we sought to understand the factors that govern the binding selectivity. We first asked the question why RAPTA compounds do not bind to the HIS site. The symmetry-related HIS (H2B H79) and HIS′ (H2B′ H79) sites are ~21 Å apart and are situated within a narrow crevice that is only accessible by diffusion through the two juxtaposed DNA gyres. To assess the full free energy profile of compound binding from bulk solvent to the binding sites, we conducted multilevel thermodynamic integration (TI) combining constrained molecular dynamics (MD) simulations at the molecular mechanics (MM) and quantum mechanics/molecular mechanics (QM/MM) levels. The MM free energy profile for RAPTA-C entry into the nucleosome crevice and approach towards the HIS site revealed a large energy barrier associated with the penetration into the confined histone binding pocket (**Figure 2a**). The free energy peaks at a distance of ~12 Å from the HIS site, where steric clashes with the bulky non-leaving ligands of RAPTA-C are prevalent. An additional barrier associated with the RAPTA-C coordination reaction at H2B H79 would further increase the energetic cost for binding to the HIS site.

Unlike RAPTA compounds, OsASN-C [(η^6-p-cymene)Os(N-phenyl-2-pyridinecarbo-thioamide)Cl] and its ruthenium equivalent, RuASN-C, both form adducts at the HIS sites in crystallographic experiments. However, the resulting RuASN-C species at H2B/H2B′ H79 appear to have their bidentate S,N-ligands (N-phenyl-2-pyridinecarbothioamide) cleaved, whereas those of OsASN-C retain both the cymene and S,N-ligands.[16] This is consistent with QM calculations performed with different DFT functionals (**Table S4**), which indicate a lower S,N-ligand binding energy for RuASN-C relative to OsASN-C when comparing the binding energies of the arene (η^6-p-cymene) and non-arene (N-phenyl-2-pyridinecarbothioamide) ligands.

Since S,N-ligand cleavage in solution is expected to influence site selectivity and

steric access, we performed MM TI simulations on OsASN-C to compare with the activity profile of RAPTA-C. Unlike RAPTA-C, OsASN-C does not display a steric challenge passing through the histone channel bottleneck, resulting in only a small increase in free energy (**Figure 2a**). Subsequent TI simulations employing a QM/MM treatment to capture the complete reaction profile (including coordination bond formation) reveal a modest overall free energy barrier of ~20 kcal/mol associated with Os coordination at the H2B H79 δ-nitrogen atom and departure of the water ligand (**Figure 2c**). The resulting OsASN-C adduct remains stable when constraints are removed and matches the crystal structure. The TI analysis shows that the differential HIS site binding activity between the RAPTA and Os/RuASN compounds arises from the presence of both arene and PTA non-leaving ligands, which create a roughly spherical and rigid steric profile. Consequently, the nucleosome crevice, which harbors a narrow access channel to the HIS site, acts as a steric site selectivity filter. Although OsASN-C and RAPTA-C have similar overall steric volumes (e.g., 1.37×10^4 $Å^3$ from a Bader's atoms in molecules analysis;[17] **Table S5**), OsASN-C exhibits greater conformational flexibility, enabling an alternative non-leaving ligand configuration that results in a flatter structural profile and facilitates its diffusion through the crevice bottleneck (**Figures 2b**, **S3**, and **Supplementary Video 1**).

In contrast to the HIS sites, the GLU and MIX sites are freely accessible from bulk solvent, as confirmed by the barrier-free approach from MM-TI up to a distance of around 6 Å from the binding sites (**Figures 3a-b**). Subsequent QM/MM TI (**Figures 3c-d**) reveals a small barrier for OsASN-C coordination at the H2A E61 carboxylate oxygen atom of the GLU site and even a lower barrier to its coordination at the H2B H106 ε nitrogen atom of the MIX site. The latter corresponds to a deep energetic minimum (−15 kcal/mol) and a final adduct configuration compatible with the crystal structure. This rationalizes the proclivity of OsASN-C for binding at the MIX site, leaving the question as to why this agent is not seen to

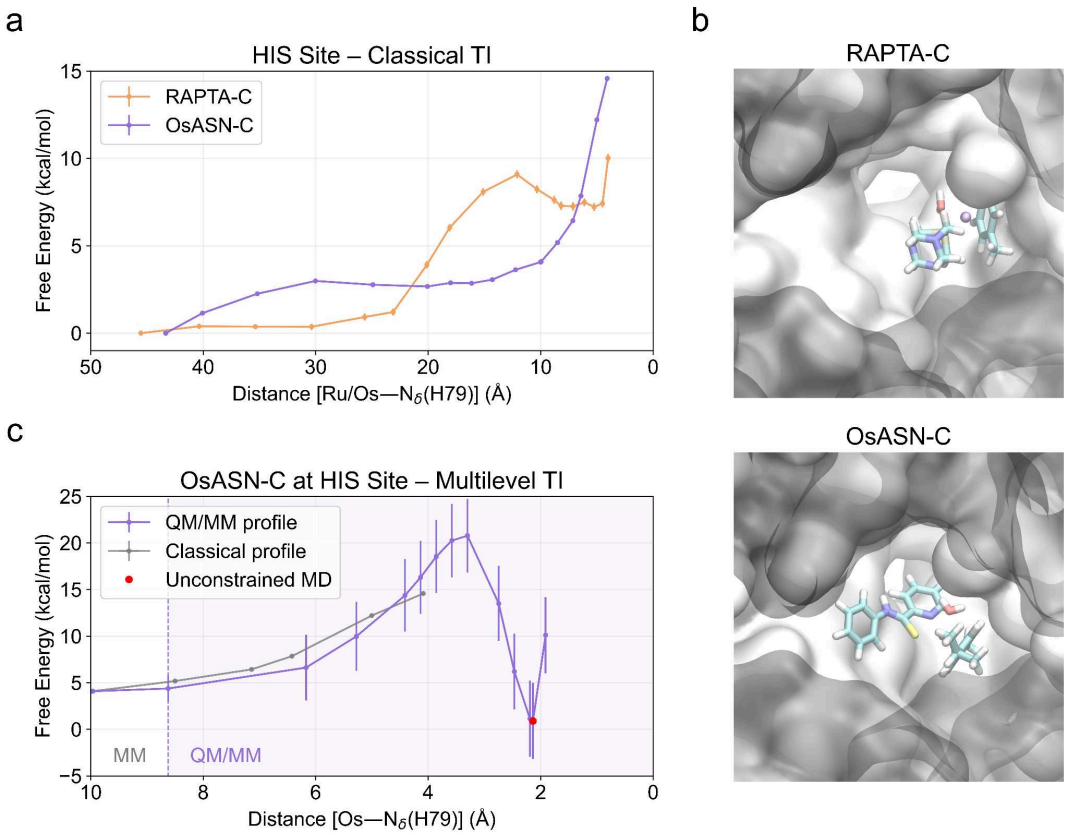

Figure 2. Binding at the HIS site for RAPTA-C and OsASN-C. **a)** Free energy profiles from classical TI. **b)** RAPTA-C and OsASN-C conformations at the entrance of the channel. Snapshot from classical TI. **c)** Multilevel free energy profile for OsASN-C, combining classical TI, QM/MM TI, and unconstrained QM/MM MD simulations. The region in which QM/MM TI is performed is highlighted with a shaded background.

bind to the adjacent GLU site in the crystallographic analyses, even though the QM/MM TI profile suggests possible binding, albeit weaker than that to the MIX site. From the configurations sampled during the MM simulations of the OsASN-C adduct at the GLU site (Os coordination at H2A E61), we observed that the adduct shows a broad range of sampled conformations. Hence, we analyzed the contacts that would result if both GLU and MIX binding sites were occupied simultaneously, showing that an adduct at the MIX site would preclude the simultaneous presence of another adduct at the GLU site (**Figure S8,** more details in the Methods section in the SI). In contrast, the same analysis for QM/MM

simulations of RAPTA-C reveals that a single adduct at the GLU site (Ru coordination at H2A E61 and H2A E64) is compatible with the simultaneous occupation of the MIX site.

The highly favorable energetics associated with OsASN-C binding at the MIX site are consistent with rapid coordination, resulting in a highly stable adduct, which consequently sterically blocks the binding of a second OsASN-C at the GLU site. On the other hand, QM/MM-TI simulations illustrate that the reaction profile of RAPTA-C binding to the GLU site is associated with an initial energetic hurdle for water ligand departure and coordination at H2A E61 (**Figure 3e**). Subsequent chelation at H2A E64 is almost spontaneous, with only a minor additional barrier of ~4 kcal/mol (**Figure 3f**), resulting in a substantial overall binding free energy of about −7 kcal/mol. This value is in excellent agreement with our earlier mass spectrometry-based measurements of RAPTA-C binding to the NCP[8,9], which yielded an overall association constant of 2.3×10^{5} M^{-1} (corresponding to a binding free energy of −7.3 kcal/mol). Apparently, the bidentate character of the end-product limits the conformational freedom of the GLU–RAPTA-C adduct, yielding an effective steric volume that does not preclude the binding of another RAPTA-C molecule to the adjacent MIX adduct (also confirmed by contact analysis, **Figure S8**).

While the coordination and non-leaving ligand character of OsASN-C precludes concurrent binding at both the GLU and MIX sites, the favored adduct at the latter location coincides with the phenyl group of the SN ligand settling into a surface niche involving van der Waals and hydrophobic contacts with histone elements of H2A and H2B (**Figure 4a** & **4b**). This added contact area contributes to the high stability of the final adduct (**Figure 3d**). Indeed, substitution of the metal center renders RuASN-C susceptible to loss of its SN ligand, and it is not observed to bind to the MIX site in the crystallographic analyses.

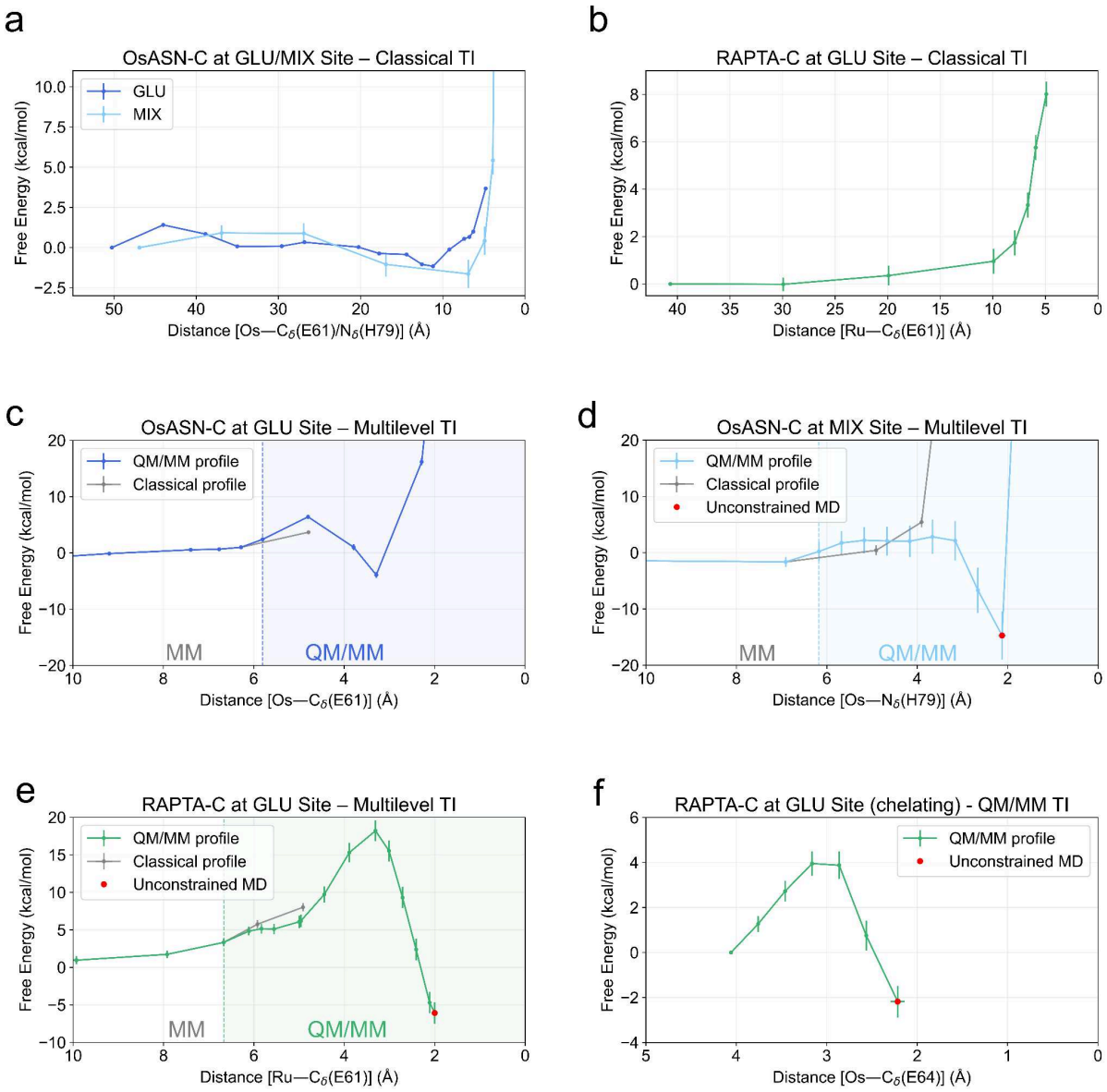

Figure 3. Free energy profiles of binding at the GLU and MIX sites for OsASN-C and RAPTA-C. **a)** OsASN-C binding at the GLU and MIX sites, classical TI. **b)** RAPTA-C binding at the GLU site, classical TI. **c)** Multilevel free energy profile of binding at the GLU site for OsASN-C. **d)** Multilevel free energy profile of binding at the MIX site for OsASN-C. **e)** Multilevel free energy profile of binding at the GLU site for RAPTA-C. **f)** QM/MM free energy profile associated with the chelation at H2A E64 upon initial (monodentate) binding at H2A E61. In c–e) the regions in which QM/MM TI is performed are highlighted with a shaded background.

While substitutions of the metal center can introduce or eliminate a particular histone binding site within the activity profile, this can also be achieved through subtle alterations in the non-leaving ligand. In our first study of a RAPTA compound binding to chromatin, RAPTA-C was observed to bind to a third electronegative surface site on the nucleosome, the EK site, in addition to the GLU and MIX locations[8] (**Figure 1a** & **1e**). At this site, the Ru ion coordinates both K59 and E63 of H4, with the cymene engaged in further van der Waals contacts with adjacent H3 residues as well as those of H2B stemming from the neighboring NCP in the crystal (**Figure 4c**).

Interested in whether RAPTA agents with different arenes would display the same site selectivity, we investigated the nucleosome binding of a RAPTA family, in which the methyl and/or isopropyl groups of the cymene are absent (benzene, [B] and toluene [T][13]), or where the cymene is replaced by 1,3,5-trimethylbenzene [3MB], 1,3,5-triisopropylbenzene [3IB], or hexamethylbenzene [6MB]. Curiously, all five agents bind the GLU site, and at least to a certain extent, the MIX site, but none associate with the EK site in the NCP crystal structures (**Figure 4d** & **Tables S1-S3**). Structural analysis reveals that the RAPTA-C cymene isopropyl group is nestled within a significantly hydrophobic niche formed by the two stacking NCPs in the crystal (**Figure 4c**). This particular group is absent in all agents except RAPTA-3I, where the additional isopropyl groups at the ortho positions likely create steric clashes with histone elements at the EK site (Figure 4e). While the increased substitutions on the arene ring, relative to cymene, associated with 3M and 6M may also pose steric challenges to binding at the EK site, this could not be the case for the B and T derivatives. Indeed, this reflects the importance of shape/hydrophobicity complementarity in adduct stability (site occupancy observed in the crystallographic analyses), as is seen for the Os/RuASN-C compounds. RAPTA-B/T are lacking the additional isopropyl-histone contacts that are available to RAPTA-C, which, moreover, is not observed to bind at the symmetry-related EK' site that is

remote from any crystal contacts.

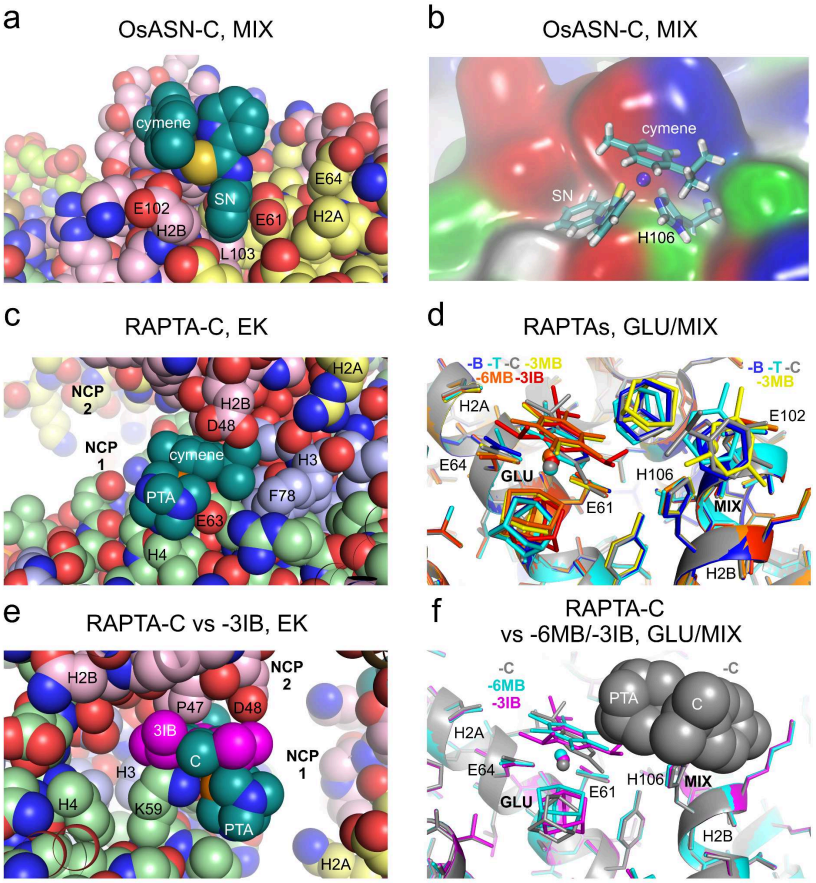

Figure 4. Non-leaving ligand shape complementarity and compatibility modulate histone site occupancy. **a,b)** Space-filling (a) and surface character (b) representations of OsASN-C binding at the MIX site (PDB ID 4J8U). The histone surface in (b) is coloured according to residue polarity (white, non-polar; blue, basic; red, acidic; green, polar). **c,e)** Space-filling representations of RAPTA-C binding at the EK site at the nucleosome–nucleosome (NCP1–NCP2) interface. In (e), 1,3,5-triisopropyl-benzene (3IB) (magenta) has been superimposed onto the RAPTA-C cymene. **d)** RAPTA-B (blue), -T (cyan), -C (grey), -3MB (yellow), -6MB (orange), and -3IB (red) binding at the GLU and (for RAPTA-B/T/C/3MB) MIX sites. The six independent NCP structures are superimposed. **f)** RAPTA-C (grey), RAPTA-6MB (cyan), and RAPTA-3IB (magenta) crystal structures, illustrating the potential steric conflict between the arene of a GLU site-bound adduct with the PTA ligand of a MIX site-bound adduct (RAPTA-C shown in space-filling) when the arene is fully-substituted (6MB) or has multiple bulky substituents (3IB). The three independent NCP structures are superimposed.

Regarding the simultaneous occupation of the GLU and MIX sites, the RAPTA-B, -T, -C, and -3M derivatives all exhibit high occupancy at both locations in the crystal structures (**Figure 4d** and **Table S3**). However, while for RAPTA-6M and RAPTA-3I there is a weak anomalous difference electron density signal at the MIX binding site, indicative of low Ru occupancy, binding at the GLU site is the major adduct, which in turn sterically precludes or substantially diminishes binding at the adjacent MIX site (**Figure 4f**). Collectively, the arene ligand identity modulates RAPTA binding in a highly arene- and histone-site-sensitive manner.

Our objective here was to understand the basis for the differential protein binding preferences within and between RAPTA and Os/RuASN agents, which display distinct profiles in associating with nucleosomal surface and crevice sites. This is crucial for determining the genomic activity of histone-targeting compounds, since binding to surface regions, such as the acidic patch, can modulate interactions with chromatin factors and neighboring nucleosomes[10,12], while binding at internal sites is likely to influence nucleosome dynamics (assembly/disassembly) alone. In summary, a picture of adduct formation potential and stability for histones emerges, and more generally proteins, in which steric factors associated with both interacting nucleosomes (i.e., chromatin) and individual nucleosomes act as initial site-discrimination filters. Metal identity and non-leaving ligand attributes modulate absolute and relative adduct stability, ultimately determining the resulting binding profiles. These principles could be crucial, for instance, in interpreting distinctions in therapeutic activities between closely related organometallic agents and for fine-tuning such compounds. For example, the dual nucleosome internal crevice/acidic patch-binder, OsASN-C, displays a distinct cancer cell line activity profile, consistent with disruption of DNA synthesis, not observed for the crevice-binding RuASN-C analogue.[16]

SUPPORTING INFORMATION

The authors have cited additional references within the Supporting Information.[18–61]

ACKNOWLEDGEMENTS

We thank V. Olieric, M. Wang, and staff for help at the Swiss Light Source (Paul Scherrer Institute, Villigen, Switzerland), M.S. Ong for assistance with X-ray data processing, and R. Muhammad for contributing to the X-ray data collection. This project was funded by the Polish National Science Center grant DEC-2024/53/B/NZ7/03477, the Singapore Ministry of Education Academic Research Fund Tier 2/3 (MOE-T2EP30121-0005, MOE2012-T3-1-001), the Singapore Ministry of Health National Medical Research Council (grant NMRC/1312/2011), and the Swiss National Science Foundation Grant Nos. 200020-185092 and 200020-219440. Computational resources from the Swiss National Computing Centre CSCS are gratefully acknowledged.

DATA AVAILABILITY

Atomic coordinates and structure factors for the crystal structures of NCP with bound RAPTA-B, -T, -C, -3MB, -6MB, and -3IB are deposited in the Protein Data Bank under accession codes 9RY3, 9RXV, 9RXU, 9RYA, 9RZK, and 9RZN, respectively. Data supporting the findings of this work are available within the article and Supplementary Information files. The computational data are available on Zenodo under https://zenodo.org/records/17258752, including Jupyter Notebooks and VMD visualization states to reproduce the analysis and generate the plots and figures presented.

COMPETING INTERESTS

The authors declare no competing interests.

AUTHOR CONTRIBUTIONS

Computational experiments, **A.L., T.E., G.P., U.R.**; X-ray crystallography, **Z.A., C.A.D.**; Compound synthesis, **A.A.N., C.G.H., P.J.D.**; Data curation, analysis, validation, and visualization, **A.L., U.R., C.A.D.**; Conceptualization, funding acquisition, project administration, and supervision, **P.J.D., U.R., C.A.D.**; Writing– original draft, **A.L., U.R., C.A.D.**; Writing– review and editing, **all authors**.

REFERENCES

[1] Nacev, B. A., Feng, L., Bagert, J. D., Lemiesz, A. E., Gao, J., Soshnev, A. A., Kundra, R., Schultz, N., Muir, T. W., & Allis, C. D. (**2019**). The expanding landscape of 'oncohistone' mutations in human cancers. *Nature*, 567, 473–478. https://doi.org/10.1038/s41586-019-1038-1

[2] Ferrand, J., Rondinelli, B., & Polo, S. E. (**2020**). Histone Variants: Guardians of Genome Integrity. *Cells*, 9(11), 2424. https://doi.org/10.3390/cells9112424

[3] Espiritu, D., Gribkova, A. K., Gupta, S., & Shaytan, A. K. (**2021**). Molecular mechanisms of oncogenesis through the lens of nucleosomes and histones. *J. Phys. Chem. B*, 125(16), 3963-3976. https://doi.org/10.1021/acs.jpcb.1c00694

[4] Bonner, E. R., Dawood, A., Gordish-Dressman, H., Eze, A., Bhattacharya, S., Yadavilli, S., Mueller, S., Waszak, S. M., & Nazarian, J. (**2023**). Pan-cancer atlas of somatic core and linker histone mutations. *NPJ Genomic Med.*, 8(1), 23. https://doi.org/10.1038/s41525-023-00367-8

[5] Zhang, W., Qu, J., Liu, G.-H., & Belmonte, J. C. I. (**2020**). The ageing epigenome and its rejuvenation. *Nat. Rev. Mol. Cell Biol.*, 21, 137-150. https://doi.org/10.1038/s41580-019-0204-5

[6] Zabransky, D. J., Jaffee, E. M., & Weeraratna, A. T. (**2022**). Shared genetic and epigenetic changes link aging and cancer. *Trends Cell Biol.*, 32(4), 338-350. https://doi.org/10.1016/j.tcb.2022.01.004

[7] Dubey, S. K., Dubey, R., & Kleinman, M. E. (**2024**). Unraveling Histone Loss in Aging and Senescence. *Cells*, 13(4), 320. https://doi.org/10.3390/cells13040320

[8] Wu, B., Ong, M. S., Groessl, M., Adhireksan, Z., Hartinger, C. G., Dyson, P. J., & Davey, C. A. (**2011**). A ruthenium antimetastasis agent forms specific histone protein adducts in the nucleosome core. *Chem. Eur. J.*, 13(17), 3562-3566. https://doi.org/10.1002/chem.201100298

[9] Adhireksan, Z., Davey, G. E., Campomanes, P., Groessl, M., Clavel, C. M., Yu, H., Nazarov, A. A., Yeo, C. H. F., Ang, W. H., Dröge, P., Rothlisberger, U., Dyson, P. J., & Davey, C. A. (**2014**). Ligand substitutions between ruthenium–cymene compounds can control protein versus DNA targeting and anticancer activity. *Nat. Commun.*, 5, 3462. https://doi.org/10.1038/ncomms4462

[10] Davey, G. E., Adhireksan, Z., Adhireksan, Z., Riedel, T., Sharma, D., Padavattan, S., Rhodes, D., Ludwig, A., Sandin, S., Murray, B. S., Dyson, P. J., & Davey, C. A. (**2017**). Nucleosome acidic patch-targeting binuclear ruthenium compounds induce aberrant chromatin condensation. *Nat. Commun.*, 8, 1575. https://doi.org/10.1038/s41467-017-01680-4

[11] Adhireksan, Z., Palermo, G., Riedel, T., Ma, Z., Muhammad, R., Rothlisberger, U., Dyson, P. J., & Davey, C. A. (**2017**). Allosteric cross-talk in chromatin can mediate drug-drug synergy. *Nat. Commun.*, 8(1), 14860. https://doi.org/10.1038/ncomms14860

[12] Batchelor, L. K., De Falco, L., von Erlach, T., Sharma, D., Adhireksan, Z., Roethlisberger, U., Davey, C. A., & Dyson, P. J. (**2019**). Crosslinking Allosteric Sites

on the Nucleosome. *Angew. Chem.*, 131(44), 15807-15811. https://doi.org/10.1002/ange.201906423

[13] Wu, B., Dröge, P., & Davey, C. A. (**2008**). Site selectivity of platinum anticancer therapeutics. *Nat. Chem. Biol.*, 4, 110–112. https://doi.org/10.1038/nchembio.2007.58

[14] Chua, E. Y. D., Davey, G. E., Fei Chin, C., Dröge, P., Han Ang, W., & Davey, C. A. (**2015**). Stereochemical control of nucleosome targeting by platinum-intercalator antitumor agents. *Nucleic Acids Res.*, 43(11), 5284-5296. https://doi.org/10.1093/nar/gkv356

[15] Ma, Z., Palermo, G., Adhireksan, Z., Murray, B. S., von Erlach, T., Dyson, P. J., Rothlisberger, U., & Davey, C. A. (**2016**). An Organometallic Compound which Exhibits a DNA Topology‐Dependent One‐Stranded Intercalation Mode. *Angew. Chem.*, 128(26), 7567-7570. https://doi.org/10.1002/ange.201602145

[16] Meier, S. M., Hanif, M., Adhireksan, Z., Pichler, V., Novak, M., Jirkovsky, E., Jakupec, M. A., Arion, V. B., Davey, C. A., Keppler, B. K., & Hartinger, C. G. (**2013**). Novel metal(II) arene 2-pyridinecarbothioamides: a rationale to orally active organometallic anticancer agents. *Chem. Sci.*, 4, 1837-1846. https://doi.org/10.1039/C3SC22294B

[16] Klose, M. H. M., Schöberl, A., Heffeter, P., Berger, W., Hartinger, C. G., Koellensperger, G., Meier-Menches, S. M., & Keppler, B. K. (**2018**). Serum-binding properties of isosteric ruthenium and osmium anticancer agents elucidated by SEC–ICP–MS. *Monatsh. Chem.*, 149, 1819-1726. https://doi.org/10.1007/s00706-018-2280-1

[17] Yu, M., & Trinkle, D. R. (**2011**). Accurate and efficient algorithm for Bader charge integration. *J. Chem. Phys.*, 134(6), 064111. https://doi.org/10.1063/1.3553716

[18] Allardyce, C. S., Dyson, P. J., Ellis, D. J., & Heath, S. L. (**2001**). [Ru(η6-p-cymene)Cl2 (pta)] (pta = 1,3,5-triaza-7-phosphatricyclo- [3.3.1.1]decane): a water soluble compound that exhibits pH dependent DNA binding providing selectivity for diseased

cells. *Chem. Commun.*, 1396-1397. https://doi.org/10.1039/B104021A

[19] Davey, C. A., Sargent, D. F., Luger, K., Maeder, A. W., & Richmond, T. J. (**2002**). Solvent Mediated Interactions in the Structure of the Nucleosome Core Particle at 1.9 Å Resolution. *J. Mol. Biol.*, 319(5), 1097-1113. https://doi.org/10.1016/S0022-2836(02)00386-8

[20] Ong, M. S., Richmond, T. J., & Davey, C. A. (**2007**). DNA stretching and extreme kinking in the nucleosome core. *J. Mol. Biol.*, 368(4), 1067-1074. https://doi.org/10.1016/j.jmb.2007.02.062

[21] Leslie, A. G. W. (**2006**). The integration of macromolecular diffraction data. *Acta Crystallogr., Sect. D: Biol. Crystallogr.*, 62(1), 48-57. https://doi.org/10.1107/s0907444905039107

[22] Evans, P. (**2006**). Scaling and assessment of data quality. *Acta Crystallogr., Sect. D: Biol. Crystallogr.*, 62, 72-82. https://doi.org/10.1107/S0907444905036693

[23] Winn, M. D., Ballard, C. C., Cowtan, K. D., Dodson, E. J., Emsley, P., Evans, P. R., Keegan, R. M., Krissinel, E. B., Leslie, A. G. W., McCoy, A., McNicholas, S. J., Murshudov, G. N., Pannu, N. S., Potterton, E. A., Powell, H. R., Read, R. J., Vagin, A. & Wilson, K. S. (**2011**). Overview of the CCP4 suite and current developments. *Acta Crystallogr., Sect. D: Biol. Crystallogr.*, 67(4), 235-242. https://doi.org/10.1107/S0907444910045749

[24] Agirre, J., Atanasova, M., Bagdonas, H., Ballard, C. B., Baslé, A., Beilsten-Edmands, J., Borges, R. J., Brown, D. G., Burgos-Mármol, J. J., Berrisford, J. M., Bond, P. S., Caballero, I., Catapano, L., Chojnowski, G., Cook, A. G., Cowtan, K. D., Croll, T. I., Debreczeni, J. Ã‰., Devenish, N. E., Dodson, E. J., Drevon, T. R., Emsley, P., Evans, G., Evans, P. R., Fando, M., Foadi, J., Fuentes-Montero, L., Garman, E. F., Gerstel, M., Gildea, R. J., Hatti, K., Hekkelman, M. L., Heuser, P., Hoh, S. W., Hough, M. A.,

Jenkins, H. T., JimÃ©nez, E., Joosten, R. P., Keegan, R. M., Keep, N., Krissinel, E. B., Kolenko, P., Kovalevskiy, O., Lamzin, V. S., Lawson, D. M., Lebedev, A. A., Leslie, A. G. W., Lohkamp, B., Long, F., Malý, M., McCoy, A. J., McNicholas, S. J., Medina, A., Millán, C., Murray, J. W., Murshudov, G. N., Nicholls, R. A., Noble, M. E. M., Oeffner, R., Pannu, N. S., Parkhurst, J. M., Pearce, N., Pereira, J., Perrakis, A., Powell, H. R., Read, R. J., Rigden, D. J., Rochira, W., Sammito, M., Sánchez Rodríguez, F., Sheldrick, G. M., Shelley, K. L., Simkovic, F., Simpkin, A. J., Skubak, P., Sobolev, E., Steiner, R. A., Stevenson, K., Tews, I., Thomas, J. M. H., Thorn, A., Valls, J. T., Uski, V., Usón, I., Vagin, A., Velankar, S., Vollmar, M., Walden, H., Waterman, D., Wilson, K. S., Winn, M. D., Winter, G., Wojdyr, M. & Yamashita, K. (**2023**). The CCP4 suite: integrative software for macromolecular crystallography. *Acta Crystallogr. D Struct. Biol.*, 79(6), 449-461. https://doi.org/10.1107/S2059798323003595

[25] Emsley, P., Lohkamp, B., Scott, W. G., & Cowtand, K. (**2010**). Features and development of Coot. *Acta Crystallogr., Sect. D: Biol. Crystallogr.*, 66(4), 486-501. https://doi.org/10.1107/S0907444910007493

[26] Murshudov, G. N., Vagin, A. A., & Dodson, E. J. (**1997**). Refinement of macromolecular structures by the maximum-likelihood method. *Acta Crystallogr., Sect. D: Biol. Crystallogr.*, *53*(3), 240-255. https://doi.org/10.1107/S0907444996012255

[27] Levy, A., Slama, V., Guilbert, S., Antalík, A., Johnson, S. K., Frisari, G., & Rothlisberger, U. (**2025**). Modeling chemical reactivity in complex systems: Insights from hybrid QM/MM MD simulations. *J. Catal.*, *453*, 116520. https://doi.org/10.1016/j.jcat.2025.116520

[28] Vock, C. A., Renfrew, A. K., Scopelliti, R., Juillerat‐Jeanneret, L., & Dyson, P. J. (**2005**). Influence of the Diketonato Ligand on the Cytotoxicities of

[Ru(η6‑p‑cymene)(R2acac)(PTA)]+ Complexes (PTA = 1,3,5‑triaza‑7‑phosphaadamantane). *Eur. J. Inorg. Chem.*, 2008(10), 1661-1671. https://doi.org/10.1002/ejic.200701291

[29] Luger, K., Mäder, A. W., Richmond, R. K., Sargent, D. F., & Richmond, T. J. (**1997**). Crystal structure of the nucleosome core particle at 2.8 Å resolution. Nature, 389, 251–260. https://doi.org/10.1038/38444

[30] Maier, J. A., Martinez, C., Kasavajhala, K., Wickstrom, L., Hauser, K. E., & Simmerling, C. (**2015**). ff14SB: Improving the Accuracy of Protein Side Chain and Backbone Parameters from ff99SB. *J. Chem. Theory Comput.*, 11(8), 3696–3713. https://doi.org/10.1021/acs.jctc.5b00255

[31] Tian, C., Kasavajhala, K., Belfon, K. A. A., Raguette, L., Huang, H., Migues, A. N., Bickel, J., Wang, Y., Pincay, J., Wu, Q., & Simmerling, C. (**2020**). ff19SB: Amino-Acid-Specific Protein Backbone Parameters Trained against Quantum Mechanics Energy Surfaces in Solution. *J. Chem. Theory Comput.*, 16(1), 528-552. https://doi.org/10.1021/acs.jctc.9b00591

[32] Pérez, A., Marchán, I., Svozil, D., Sponer, J., Cheatham, T. E., Laughton, C. A., & Orozco, M. (**2007**). Refinement of the AMBER force field for nucleic acids: improving the description of α/γ conformers. *Biophys. J.*, 92(11), 3817-3829. https://doi.org/10.1529/biophysj.106.097782

[33] Jorgensen, W. L., Chandrasekhar, J., Madura, J. D., Impey, R. W., & Klein, M. L. (1983). Comparison of simple potential functions for simulating liquid water. *J. Chem. Phys.*, 79, 926-935. https://doi.org/10.1063/1.445869

[34] Gossens, C., Tavernelli, I., & Rothlisberger, U. (**2008**). DNA Structural Distortions Induced by Ruthenium−Arene Anticancer Compounds. *J. Am. Chem. Soc.*, 130(33), 10921–10928. https://doi.org/10.1021/ja800194a

[35] Desoize, B. (**2004**). Metals and metal compounds in cancer treatment. *Anticancer Res.*, 24(3A), 1529-1544.

[36] Scolaro, C., Hartinger, C. G., Allardyce, C. S., Keppler, B. K., & Dyson, P. J. (**2008**). Hydrolysis study of the bifunctional antitumour compound RAPTA-C,[Ru (η6-p-cymene) Cl2 (pta)]. *J. Inorg. Biochem.*, 102(9), 1743-1748. https://doi.org/10.1016/j.jinorgbio.2008.05.004

[37] Abraham, M. J., Murtola, T., Schulz, R., Páll, S., Smith, J. C., Hess, B., & Lindahl, E. (**2015**). GROMACS: High performance molecular simulations through multi-level parallelism from laptops to supercomputers. *SoftwareX*, 1, 19-25. https://doi.org/10.1016/j.softx.2015.06.00

[38] Van Der Spoel, D., Lindahl, E., Hess, B., Groenhof, G., Alan, M. E., & Berendsen, H. J. C. (**2005**). GROMACS: fast, flexible, and free. *J. Comput. Chem.*, 26(16), 171-1718. https://doi.org/10.1002/jcc.20291

[39] Berendsen, H. J. C., van der Spoel, D., & van Drunen, R. (**1995**). GROMACS: A message-passing parallel molecular dynamics implementation. *Comput. Phys. Commun.*, 91(1-3), 43-56. https://doi.org/10.1016/0010-4655(95)00042-E

[40] CPMD [Copyright IBM Corp 1990-2008, Copyright MPI für Festkörperforschung Stuttgart 1997-2001]. (https://github.com/CPMD-code)

[41] Laio, A., VandeVondele, J., & Rothlisberger, U. (**2002**). A Hamiltonian electrostatic coupling scheme for hybrid Car–Parrinello molecular dynamics simulations. *J. Chem. Phys.*, 116, 6941–6947. https://doi.org/10.1063/1.1462041

[42] Becke, A. D. (**1988**). Density-functional exchange-energy approximation with correct asymptotic behavior. *Phys. Rev. A*, 38, 3098. https://doi.org/10.1103/PhysRevA.38.3098

[43] Lee, C., Yang, W., & Parr, R. G. (**1988**). Development of the Colle-Salvetti

correlation-energy formula into a functional of the electron density. *Phys. Rev. B*, 37(2), 785. https://doi.org/10.1103/PhysRevB.37.785

[44] Troullier, N., & Martins, J. L. (**1991**). Efficient pseudopotentials for plane-wave calculations. *Phys. Rev. B*, 43, 1993. https://doi.org/10.1103/PhysRevB.43.1993

[45] von Lilienfeld, A. O., Tavernelli, I., Rothlisberger, U., & Sebastiani, D. (**2004**). Optimization of Effective Atom Centered Potentials for London Dispersion Forces in Density Functional. *Theory. Phys. Rev. Lett*., 93(15), 153004. https://doi.org/10.1103/PhysRevLett.93.153004

[46] Nosé, S. (**1985**). Canonical dynamics: Equilibrium phase-space distributions. *Phys. Rev. A*, 31 1695–1697. https://doi.org/10.1080/00268970110089108

[47] Hoover, V. G. (**1998**). Free energy from constrained molecular dynamics. *J. Chem. Phys.*, 109, 7737-7744. https://doi.org/10.1103/PhysRevA.31.1695

[48] Carter, E. A., Ciccotti, G., Hynes, J. T., & Kapral, R. (**1989**). Constrained reaction coordinate dynamics for the simulation of rare events. *Chem. Phys. Lett.*, 156(5), 472-477. https://doi.org/10.1016/S0009-2614(89)87314-2

[49] Sprik, M., & Ciccotti, G. (**1998**). Free energy from constrained molecular dynamics. *J. Chem. Phys.*, 109, 7737-7744. https://doi.org/10.1063/1.477419

[50] Maragliano, L., Ferrario, M., & Ciccotti, G. (**2004**). Effective Binding Force Calculation in Dimeric Proteins. *Mol. Simul.*, 30(11-12), 807-816. https://doi.org/10.1080/0892702042000270205

[51] Hirakawa, T., Bowler, D. R., Miyazaki, T., Morikawa, Y., & Truflandier, L. A. (**2020**). Blue moon ensemble simulation of aquation free energy profiles applied to mono and bifunctional platinum anticancer drugs. *J. Comput. Chem*., 41(22), 1973-1984. https://doi.org/10.1002/jcc.26367

[52] Bruessel, M., Di Dio, P. J., Muniz, K., & Kirchner, B. (**2011**). Comparison of Free

Energy Surfaces Calculations from Ab Initio Molecular Dynamic Simulations at the Example of Two Transition Metal Catalyzed Reactions. *Int. J. Mol. Sci.*, 12(2), 1389-1409. https://doi.org/10.3390/ijms12021389

[53] Borišek, J., & Magistrato, A. (**2020**). All-Atom Simulations Decrypt the Molecular Terms of RNA Catalysis in the Exon-Ligation Step of the Spliceosome. *ACS Catal.,* 10(9), 5328-5334. https://doi.org/10.1021/acscatal.0c00390

[54] Casalino, L., Nierzwicki, Ł., Jinek, M., & Palermo, G. (**2020**). Catalytic mechanism of non-target DNA cleavage in CRISPR-Cas9 revealed by ab initio molecular dynamics. *ACS Catal.*, 10(22), 13596-13605. https://doi.org/10.1021/acscatal.0c03566

[55] De Vivo, M., Dal Peraro, M., & Klein, M. L. (**2008**). Phosphodiester Cleavage in Ribonuclease H Occurs via an Associative Two-Metal-Aided Catalytic Mechanism. J. *Am. Chem. Soc.*, 130(33), 10955-10962. https://doi.org/10.1021/ja8005786

[56] Humphrey, W., Dalke, A., & Schulten, K. (**1996**). VMD: visual molecular dynamics. *J. Mol. Graphics*, 14(1), 33-38. https://doi.org/10.1016/0263-7855(96)00018-5

[57] Vosko, S. H., Wilk, L., & Nusair, M. (**1980**). Accurate spin-dependent electron liquid correlation energies for local spin density calculations: a critical analysis. *Can. J. Phys.*, 58(8), 1200-1211. https://doi.org/10.1139/p80-159

[58] Stephens, P. J., Devlin, F. J., Chabalowski, C. F., & Frisch, M. J. (**1994**). Ab initio calculation of vibrational absorption and circular dichroism spectra using density functional force fields. *J. Phys. Chem.*, 98(45), 11623-11627. https://doi.org/10.1021/j100096a001

[59] Zhao, Y., & Truhlar, D. G. (**2008**). The M06 suite of density functionals for main group thermochemistry, thermochemical kinetics, noncovalent interactions, excited states, and transition elements: two new functionals and systematic testing of four M06-class functionals and 12 other functionals. *Theor. Chem. Acc.,* 120(1), 215-241.

http://dx.doi.org/10.1007/s00214-007-0401-8

[60] Zhao, Y., & Truhlar, D. G. (**2006**). A new local density functional for main-group thermochemistry, transition metal bonding, thermochemical kinetics, and noncovalent interactions. *J. Chem. Phys.*, 125(19). https://doi.org/10.1063/1.2370993

[61] Frisch, M. J., Trucks, G. W., Schlegel, H. B., Scuseria, G. E., Robb, M. A., Cheeseman, J. R., Scalmani, G., Barone, V., Mennucci, B., Petersson, G. A., Nakatsuji, H., Caricato, M., Li, X., Hratchian, H. P., Izmaylov, A. F., Bloino, J., Zheng, G., Sonnenberg, J. L., Hada, M., Ehara, M., Toyota, K., Fukuda, R., Hasegawa, J., Ishida, M., Nakajima, T., Honda, Y., Kitao, O., Nakai, H., Vreven, T., Montgomery, J. A., Jr., Peralta, J. E., Ogliaro, F., Bearpark, M., Heyd, J. J., Brothers, E., Kudin, K. N., Staroverov, V. N., Kobayashi, R., Normand, J., Raghavachari, K., Rendell, A., Burant, J. C., Iyengar, S. S., Tomasi, J., Cossi, M., Rega, N., Millam, J. M., Klene, M., Knox, J. E., Cross, J. B., Bakken, V., Adamo, C., Jaramillo, J., Gomperts, R., Stratmann, R. E., Yazyev, O., Austin, A. J., Cammi, R., Pomelli, C., Ochterski, J. W., Martin, R. L., Morokuma, K., Zakrzewski, V. G., Voth, G. A., Salvador, P., Dannenberg, J. J., Dapprich, S., Daniels, A. D., Farkas, Ö., Foresman, J. B., Ortiz, J. V., Cioslowski, J., Fox, D. J. (**2010**). Gaussian 09, Revision C.01. Gaussian, Inc., Wallingford CT.

Supporting Information:

Tuning Histone Site Selectivity in the Nucleosome with Organometallic Agents

Andrea Levy[1], Zenita Adhireksan[2,3], Thibaud von Erlach[1], Giulia Palermo[1*],

Alexey A. Nazarov[4], Christian G. Hartinger[5], Paul J. Dyson[4],

Ursula Rothlisberger[1#] & Curtis A. Davey[2,3,6#]

[1] Laboratory of Computational Chemistry and Biochemistry, Ecole Polytechnique Fédérale de Lausanne, Lausanne CH-1015, Switzerland

[2] School of Biological Sciences, Nanyang Technological University, 60 Nanyang Drive, Singapore 637551

[3] NTU Institute of Structural Biology, Nanyang Technological University, 59 Nanyang Drive, Singapore 636921

[4] Institute of Chemical Sciences and Engineering, École Polytechnique Fédérale de Lausanne (EPFL), Lausanne, 1015 Switzerland

[5] School of Chemical Sciences, University of Auckland, Private Bag 92019, Auckland 1142, New Zealand

[6] Małopolska Centre of Biotechnology, Jagiellonian University, 31-007 Kraków, Poland

[*] Present address: Department of Bioengineering and Department of Chemistry, University of California Riverside, 900 University Avenue, Riverside, CA, 52512, USA

[#] Corresponding authors: U.R. (ursula.roethlisberger@epfl.ch), C.A.D. (curtis.davey@uj.edu.pl)

Atomic coordinates and structure factors for the crystal structures of NCP with bound RAPTA-B, -T, -C, -3MB, -6MB, and -3IB are deposited in the Protein Data Bank under accession codes 9RY3, 9RXV, 9RXU, 9RYA, 9RZK, and 9RZN, respectively. Data supporting the findings of this work are available within the article and Supplementary Information files. The computational data are available on Zenodo under https://zenodo.org/records/17258752, including Jupyter Notebooks and VMD visualization states to reproduce the analysis and generate the plots and figures presented.

EXPERIMENTAL SECTION

Ruthenium compound synthesis

RAPTA agents having different arene ligands were synthesized as described previously[18]. In brief, for the synthesis of RAPTA-C as an example, equimolar amounts of 1,3,5-triaza-7-phosphatricyclo[3.3.1.1]decane and $[Ru(\eta^6\text{-}p\text{-cymene})Cl_2]_2$ were refluxed in methanol, and the product was precipitated by addition of diethyl ether. The purity of the prepared products was confirmed through elemental analysis.

Crystallographic analysis of RAPTA-treated nucleosome

NCP crystals were produced and transferred into a stabilizing harvest buffer (37 mM $MnCl_2$, 40 mM KCl, 20 mM K-cacodylate [pH 6.0], 24% [v/v] 2-methyl-2,4-pentanediol, and 2% [w/v] trehalose) as previously described.[19,20] The 37 mM $MnCl_2$ and 40 mM KCl buffer components were subsequently eliminated by gradual replacement with 10 mM $MgSO_4$, followed by thorough rinsing of crystals with the $MgSO_4$-containing buffer to remove any residual Mn^{2+} and Cl^-.[8] The crystallographic analyses reported here stem from varied-duration incubations of NCP crystals with a 0.25–1.0 mM concentration of a given RAPTA compound included in the buffer (as outlined in **Tables S2 & S3**).

Single-crystal X-ray diffraction data were recorded as described previously[9], with crystals mounted directly into the cryocooling N_2 gas stream set at −175 °C, using beam lines X06SA or X06DA of the Swiss Light Source (Paul Scherrer Institute, Villigen, Switzerland) and an X-ray wavelength of 1.5 Å. Data were processed with MOSFLM[21] and SCALA[22] from the CCP4 package.[23,24] The native NCP models (PDB codes 2NZD and 3REH [20,8]) and NCP with bound RAPTA-C (PDB code 3MNN[8]) and RAPTA-T (PDB code 5DNM[11]) were used for initial structure solution by molecular replacement and comparative analysis.

Structural refinement and model building were carried out with the COOT[25] and REFMAC[26] programs from the CCP4 suite.[23,24]

Refinement restraint parameters for the RAPTA species were based on the small-molecule crystal structures [18,27] and included bond length restraints to the coordinating histone groups. The RAPTA-C and RAPTA-T structures described here differ from those reported earlier[8,11] by virtue of the imposition of bonding restraints to the coordinating glutamate, histidine, and/or lysine groups as well as extension of the diffraction data resolution. Graphic figures were prepared with PyMOL (DeLano Scientific LLC, San Carlos, CA, USA). Data collection and structure refinement statistics are given in **Tables S1** and **S2**.

COMPUTATIONAL METHODS

Models for computational investigations

The system preparation and force field parameters were chosen similarly to previous studies on the same system.[9,11,XX] In brief, the apo system was initially obtained by refining the structure of the native NCP solved at 2.80 Å resolution (PDB code 1AOI[29]) and modeled with the AMBER force field ff14SB[30,31] with the ff99bsc0 modifications for DNA.[32] The TIP3P model[33] was employed for the description of explicit waters, with the addition of Na+ counterions to neutralize the total charge, leading to a total number of more than ~200'000 atoms. The parameters for the different drugs were adapted from previous studies.[34] As aquation is a process happening spontaneously in the cell medium[35,36] (activating, therefore, the prodrug), the simulations were initiated with a monoaquated, positively charged version of RAPTA-C. Similarly, experimental results have shown that the aquation of the OsASN-C compound is a thermodynamically favorable reaction, and also in this case, the aquated version of the compound has been simulated, using the R-enantiomer, which is the dominant adduct observed in the crystal structure.

Classical MD simulations were performed with GROMACS,[37–39] heating the apo system to 300K (NVT ensemble), and then equilibrating for hundreds of ns in the NPT ensemble. Then, the different drugs were added to the bulk solvent away (~40Å) from the system and let equilibrate. The distance between the drug and the target location has then been constrained to perform thermodynamic integration (discussed in more detail in the next section) and decreased systematically. Every frame has been equilibrated, and the trajectory has been used to calculate the corresponding force due to the distance constraint. For each window, at least ~10ns were simulated, or until the constraint forces converged to their average values.

Born–Oppenheimer (BO) QM/MM MD simulations were performed with CPMD[40] with the QM/MM electrostatic embedding scheme by Laio et al.[41]. Simulations were started from a configuration from a previous constrained MD run at the MM level. The QM level of choice was Density Functional Theory (DFT), using the BLYP functional[42,43] with norm-conserving Martins-Trouiller pseudopotentials[44] and correcting the exchange-correlation functional through the use of properly parameterized Dispersion Corrected Atom-Centered Potentials.[45] The atoms treated at the QM level include the drug and the binding amino acid side chains, i.e., H2A E61 and H2A E64 for the GLU site, H2B H106 and H2B E102 for the MIX site, and H2B H79 for the HIS site. The bonds crossing the QM–MM boundary have been treated with monovalent pseudopotentials on the C_α atoms. Wavefunctions were expanded in a plane wave basis with a cutoff of 70Ry for RAPTA-C, and 100Ry for OsASN-C. The QM/MM simulations consisted of an initial wavefunction optimization, followed by thermalization of the system at 300 K. Then Born–Oppenheimer (BO) MD simulations were carried out with a timestep of $10\hbar/E_h$ (~0.24 fs). The QM and the MM subsystems were thermostated by three separate chains of Nosé–Hoover thermostats,[46,47] for the QM atoms, the NCP, and the solvent, respectively. Analogously to

the MM case, the distance between the drug and the target location has been successively constrained to perform thermodynamic integration. For each window, at least ~1ps were simulated, or until the constraint forces converged to their average values.

Multilevel thermodynamic integration

Thermodynamic integration (TI) is a well-established method for free energy calculations from molecular dynamics simulations.[48,49] In brief, the free energy difference along a reaction path defined by varying a reaction coordinate ξ can be obtained as

$$G(\xi) - G(\xi_0) = \int_{\xi_0}^{\xi} d\xi' \langle \frac{\partial H}{\partial \xi} \rangle_{\xi'}^{cond.},$$

where $\langle \dots \rangle_{\xi'}^{cond.}$ indicates a conditional average evaluated at $\xi(\boldsymbol{r}) = \xi'$, which can be conveniently evaluated in the so-called blue-moon ensemble as the time average over a constrained trajectory, taking into account an additional factor to compensate for the bias introduced by the constraint. However, if the reaction coordinate is chosen as the distance between two atoms i and j, i.e. $\xi = |\boldsymbol{r}_i - \boldsymbol{r}_j|$, the equations become simpler and the mean force can be directly estimated from the time average of the constraint force without the need for reweighting or correction terms.

TI within the blue moon ensemble has been extensively applied to MD simulations at MM[50], QM[51,52], and QM/MM level.[53–55] The approach we propose in this work, *multilevel TI*, is a combination of an MM TI performed at large distances, where long sampling time is needed to ensure convergence of the constraint force, together with a QM/MM TI at short distances, where the MM description is not accurate enough and is not able to describe, e.g., bond breaking or formation. The total profile is obtained by combining the constraint forces before performing the integration to get the free energy, assuming that for large enough distances, the constraint forces from an MM-only simulation and a QM/MM one should

match. This can be verified by always ensuring an overlapping region between the constrained distances studied at MM and QM/MM levels, enabling us to verify that the profile from the QM/MM forces is similar to or lower than the MM one in the overlap region.

The main advantage of multilevel TI is the possibility of getting a full free energy profile, from the bulk solvent to the binding site. Moreover, performing MM TI first allows us to get information about free energy barriers involved in accessing a putative binding site. If the free energy barrier from MM TI is already large, it is not helpful to proceed with a long and computationally costly QM/MM TI, since the binding site is unlikely to be reached in the first place. This is in line with the philosophy of the QM/MM approach of focusing the computational effort where it is strictly needed.

Contact analysis

We performed a contact analysis with an in-house Python code distributed in a Jupyter Notebook (deposited on Zenodo https://zenodo.org/records/17258752). The analysis consists of using a fixed structure as a reference, and conformations from the MD, and computing for each frame the distance for the closest contact, i.e. lowest distance among atoms of the reference structure vs MD, and the number of contacts, i.e. the number of atoms of the two structures with distances lower than a threshold (2.0Å in this case). Before the contact analysis, we aligned the conformations from the MD to the crystal structure based on Cα carbons of the protein using VMD.[56] Then we extracted the reference conformation of the drug at the MIX site and the conformations of the drug at the GLU site from the MD simulations.

Binding energy QM calculations

To compute the influence of the Ru vs Os metal center at the HIS site, we computed the energy of binding for RuASN-C and OsASN-C compounds with QM calculations on a minimal QM model of the system, composed of the drug and the binding histidine. More details, together with the results for all reactants and products selected, are reported in the Supporting Information. Briefly, to compute the binding energy of the arene compound, we used as reactants the arene itself and the non-arene compound with Ru/Os bound to histidine, and as product Ru/OsASN-C bound to histidine. Similarly, for the binding energy of the non-arene compounds, we used the non-arene compound and the arene one bound to histidine as reactants, and Ru/OsASN-C bound to histidine as the product.

We compared results with different DFT functionals, namely BLYP[42,43], B3LYP[42,43,57,58], M06[59], and M06L[60], while performing a full geometry optimization on the different reactants and products using a 6-31G* basis set and LANL2DZ pseudopotentials to describe the transition metal. The calculations have been performed using Gaussian 09.[61]

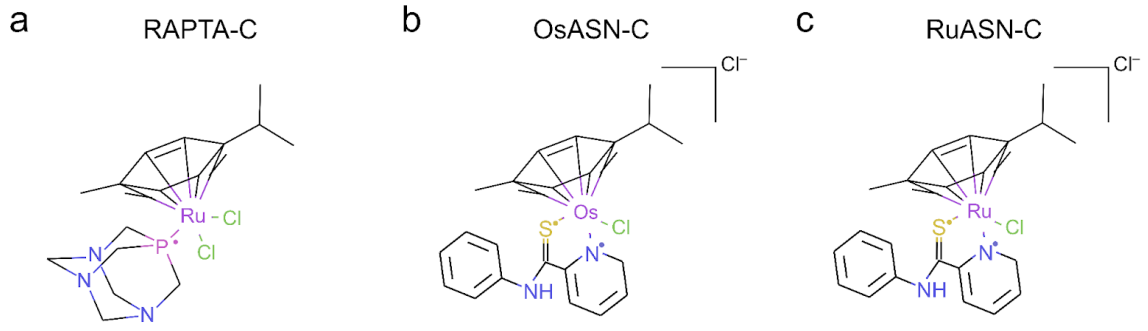

Figure S1. Schematic representation of the RAPTA-C (a), OsASN-C (b), and RuASN-C (c) compounds. For the computational studies, the aquated version of the compounds has been used, with a total charge of +1 for the monoaquated RAPTA-C and +2 for the aquated Os/RuASN-C compounds.

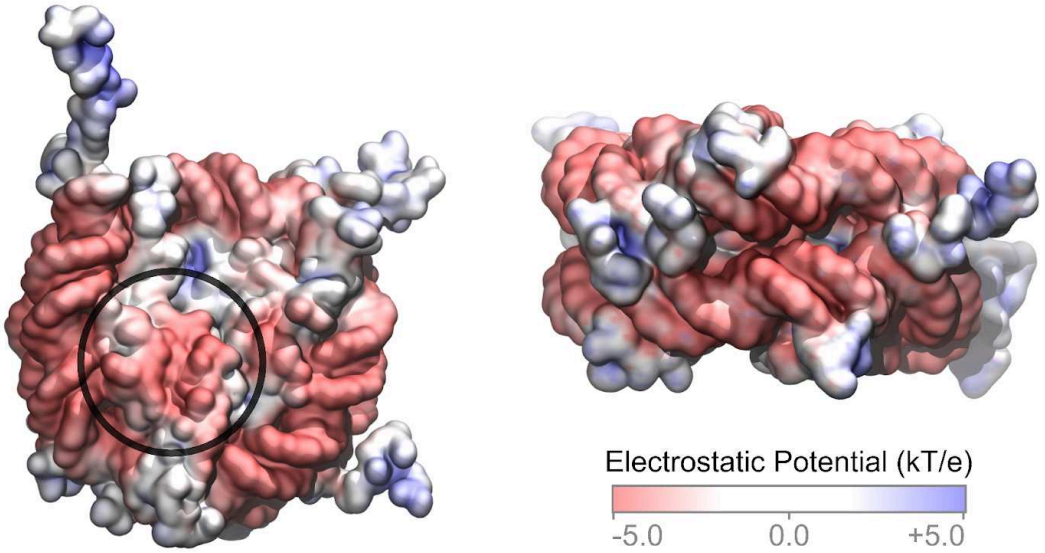

Figure S2. Electrostatic potential surface for the nucleosome core particle (NCP; PDB ID 1KX5) computed with APBS VMD plugin, after protonation with H++ server (http://newbiophysics.cs.vt.edu/H++/). The acidic patch is highlighted with a black circle.

Table S1. Data collection and refinement statistics for NCP treated with RAPTA agents.

	RAPTA-B	**RAPTA-T**	**RAPTA-C**
Data collection			
Space group	$P2_12_12_1$	$P2_12_12_1$	$P2_12_12_1$
Cell dimensions			
a (Å)	106.68	106.68	106.35
b (Å)	110.01	109.82	109.86
c (Å)	182.43	182.34	182.59
Resolution (Å)	2.75–48.9 (2.75–2.90)	2.60–60.8 (2.60–2.74)	2.30–94.1 (2.30–2.42)
R_{merge} (%)	4.5 (124)	6.1 (95.1)	7.2 (103)
R_{pim} (%)	2.3 (78.3)	2.8 (71.5)	3.8 (89.5)
$I/\sigma I$	20.1 (1.0)	13.2 (1.0)	8.6 (0.7)
Completeness (%)	99.6 (98.0)	88.4 (55.3)	96.5 (80.2)
CC½ (%)	100 (44.7)	99.9 (40.8)	99.4 (57.6)
Redundancy	6.0 (4.0)	6.2 (3.1)	4.8 (2.4)
Refinement			
Resolution (Å)	2.75–48.9	2.60–58.7	2.30–94.1
No. reflections	55,054	57,440	90,236
R_{work} / R_{free} (%)	22.0 / 26.9	21.9 / 24.2	22.7 / 25.6
No. atoms	12,075	12,077	12,126
B-factors (Å^2)	115	102	91.7
R.m.s. deviations			
Bond lengths (Å)	0.004	0.004	0.004
Bond angles (°)	1.38	1.31	1.41

Single crystal data sets. Values in parentheses are for the highest resolution shell.
RAPTA-B: 19-hour incubation of NCP crystal with a 1 mM concentration of RAPTA-B.
RAPTA-T: 20-hour incubation of NCP crystal with a 0.25 mM concentration of RAPTA-T.[11]
RAPTA-C: 56-hour incubation of NCP crystal with a 0.75 mM concentration of RAPTA-C.[8]

Table S2. Data collection and refinement statistics for NCP treated with RAPTA agents.

	RAPTA-3MB	**RAPTA-6MB**	**RAPTA-3IB**
Data collection			
Space group	$P2_12_12_1$	$P2_12_12_1$	$P2_12_12_1$
Cell dimensions			
a (Å)	106.86	107.11	106.78
b (Å)	109.91	110.03	109.90
c (Å)	182.44	182.33	182.34
Resolution (Å)	2.70–48.9 (2.70–2.85)	2.99–76.7 (2.99–3.15)	2.70–76.6 (2.70–2.85)
R_{merge} (%)	4.0 (115)	6.4 (93.0)	9.8 (77.2)
R_{pim} (%)	2.0 (66.9)	3.3 (61.7)	4.9 (54.6)
$I/\sigma I$	24.5 (1.1)	11.3 (1.2)	8.6 (1.1)
Completeness (%)	96.9 (80.6)	99.3 (95.7)	86.4 (47.9)
CC½ (%)	100 (60.9)	99.7 (55.8)	98.6 (49.2)
Redundancy	6.0 (4.0)	5.4 (3.3)	5.2 (2.8)
Refinement			
Resolution (Å)	2.70–48.9	2.99–70.8	2.70–76.6
No. reflections	56,715	43,044	50,290
R_{work} / R_{free} (%)	21.8 / 27.2	21.8 / 26.8	23.0 / 29.1
No. atoms	12,081	12,064	12,067
B-factors (Å^2)	110	122	102
R.m.s. deviations			
Bond lengths (Å)	0.004	0.004	0.004
Bond angles (°)	1.40	1.46	1.35

Single crystal data sets. Values in parentheses are for the highest resolution shell.
RAPTA-3MB: 3-hour incubation of NCP crystal with a 1 mM concentration of RAPTA-3MB.
RAPTA-6MB: 4-hour incubation of NCP crystal with a 1 mM concentration of RAPTA-6MB.
RAPTA-3IB: 21-hour incubation of NCP crystal with a 1 mM concentration of RAPTA-3IB.

Table S3. Ruthenium(II) binding sites in NCP treated with the RAPTA agents.

	Anomalous Difference Peak Height (σ)		
Agent	**GLU**	**MIX**	**EK**
RAPTA-B	7.7	7.0	- -
RAPTA-T	6.8	6.1	- -
RAPTA-C	9.4	6.6	8.3
RAPTA-3MB	7.2	6.2	- -
RAPTA-6MB	5.6	3.4	- -
RAPTA-3IB	7.8	3.4	- -

Values correspond to anomalous difference electron density map peak magnitudes >3.0σ at the GLU, MIX, and EK sites.

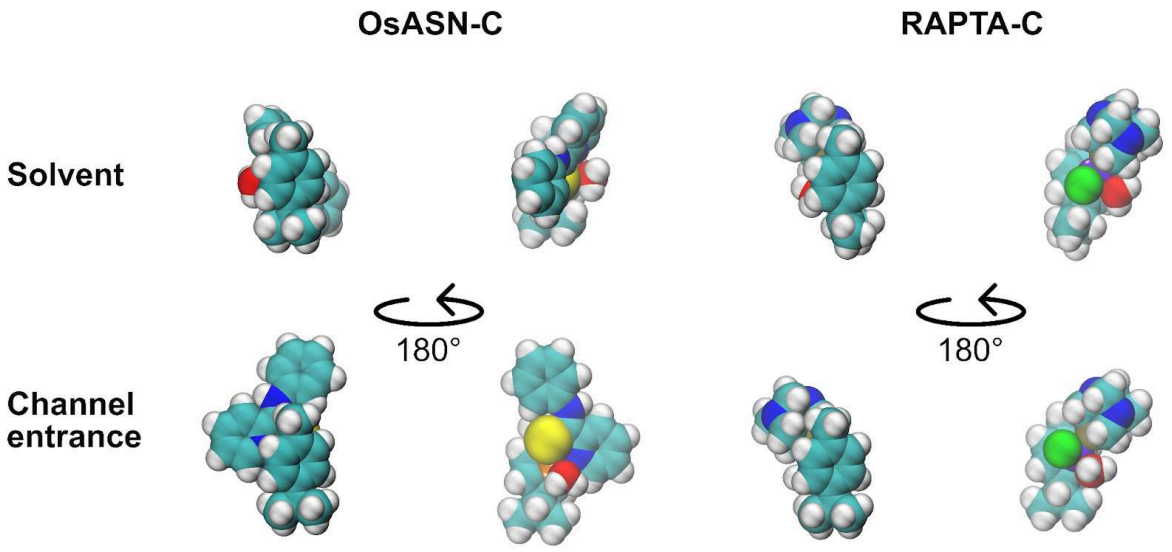

Figure S3. Comparison between compound conformation in the solvent vs at the channel entrance. The conformation has been extracted from TI windows at 40Å (solvent) and 12Å (channel entrance).

Table S4. Binding energies for the arene and non-arene ligands in RuASN-C vs OsASN-C compounds obtained with different DFT functionals.

Binding energy (kcal/mol)	Compound	**BLYP**	**B3LYP**	**M06**	**M06L**
Arene	**Ru**ASN-C	-8.35	-11.28	-35.86	-36.38
	OsASN-C	-25.85	-32.87	-56.64	-57.62
	ΔΔE (Ru-Os)	**17.50**	**21.59**	**20.77**	**21.24**
Non arene	**Ru**ASN-C	-30.62	-34.99	-44.94	-48.76
	OsASN-C	-40.95	-46.73	-55.18	-59.41
	ΔΔE (Ru-Os)	**10.33**	**11.74**	**10.24**	**10.65**

Table S5. Results from Bader's atom in molecule analysis for RAPTA-C and OsASN-C. For each compound, a representative conformation from the TI window at 40Å was extracted, where the ligand is in the solvent. From the conformation, we generated a cube file containing the electron density generated using the same parameters as those in the subsequent QM/MM simulations and analysed them with the Bader Charge Analysis code (Version 1.05 08/19/23, available at https://theory.cm.utexas.edu/henkelman/code/bader/).

	RAPTA-C	**OsASN-C**
Number of atoms	51	53
Grid size	241 × 241 × 241	241 × 241 × 241
Number of Bader maxima	221,123	240,632
Significant maxima	108	112
Total number of electrons	141.0000	151.0000
Vacuum charge	0.0000	0.0000

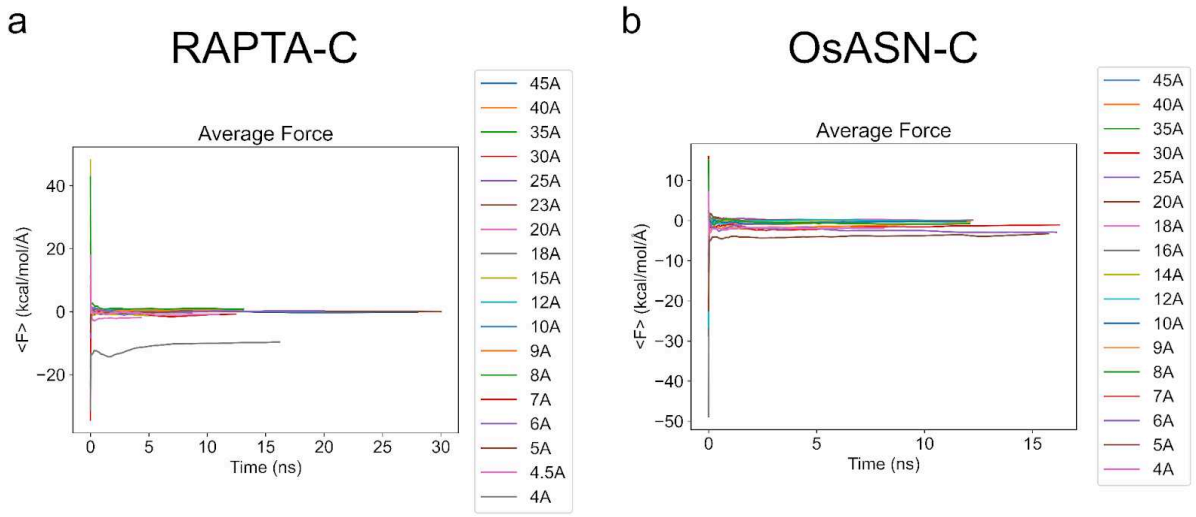

Figure S4. Convergence of the average force in the classical TI of the binding to the HIS site for RAPTA-C (a) and OsASN-C (b).

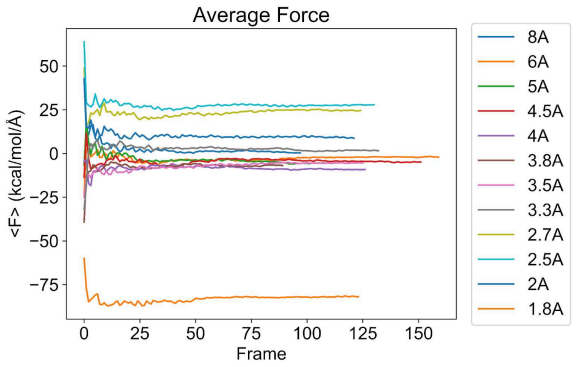

Figure S5. Convergence of the average force in the QM/MM TI of the binding to the HIS site for OsASN-C.

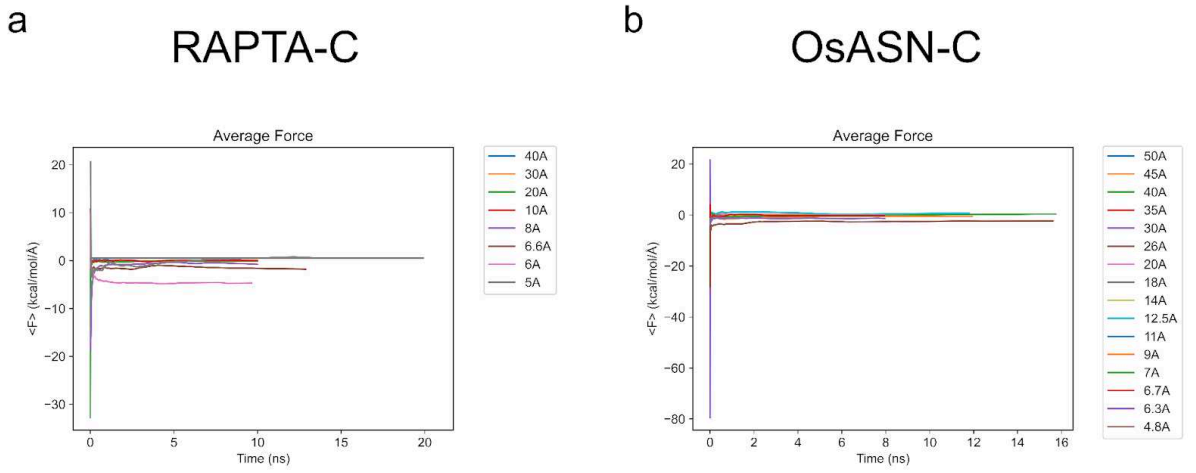

Figure S6. Convergence of the average force in the classical TI of the binding to the GLU site for RAPTA-C (a) and OsASN-C (b).

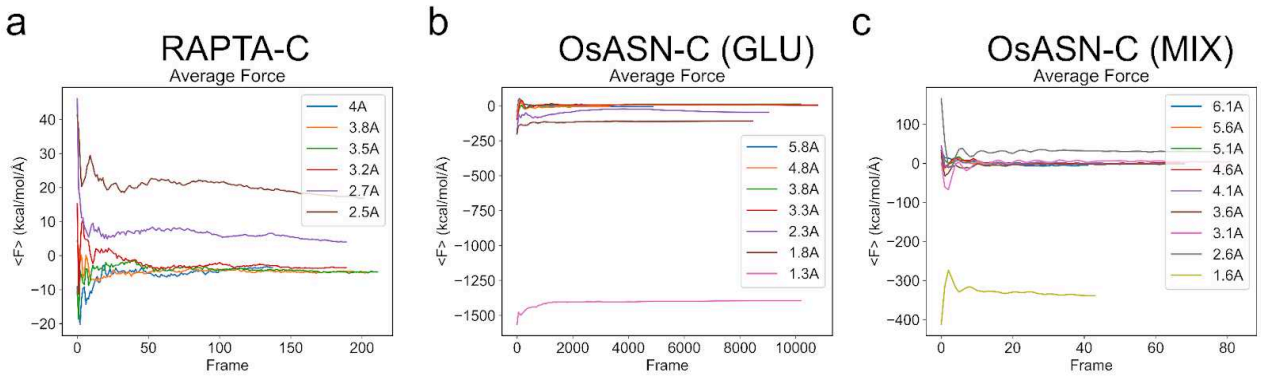

Figure S7. Convergence of the average force in the QM/MM TI of the binding for RAPTA-C to the GLU site (a), OsASN-C to the GLU site (b), and OsASN-C to the MIX site (c).

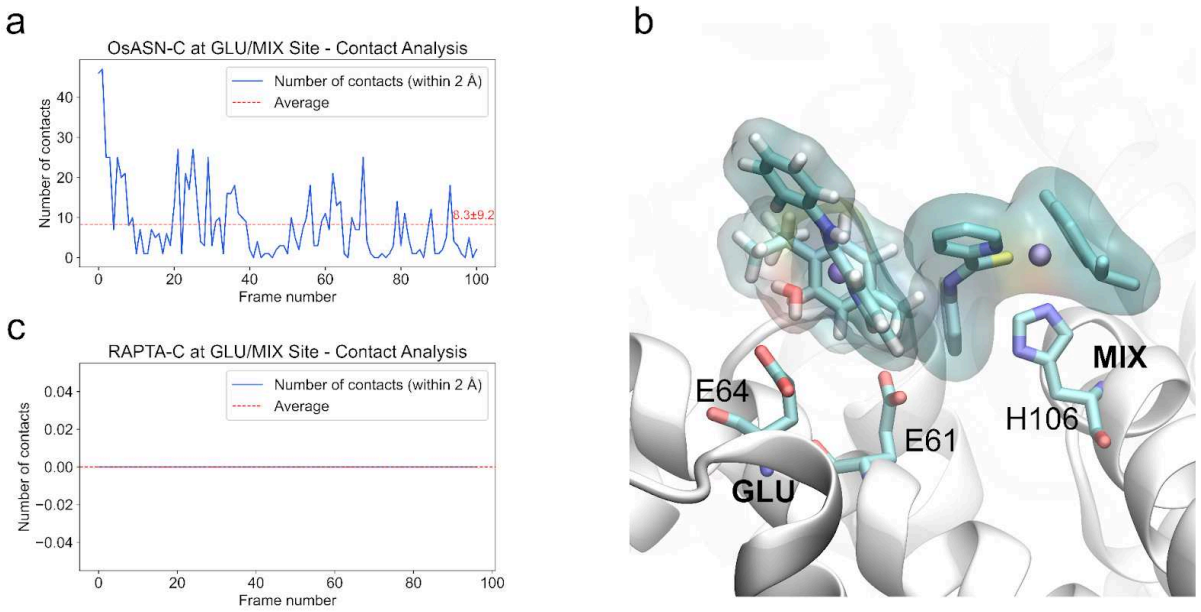

Figure S8. Contact analysis of the conformations at the GLU site with respect to the crystal structure having an OsASN-C adduct at the MIX site. **a)** OsASN-C close contacts. The average number of contacts (8.3±9.2 short atomic contacts ≤2.0 Å) is shown in red. The average close contact distance is 1.3±0.8 Å. **b)** Representative snapshot from the classical TI at the minimum aligned to the crystal structure with the MIX site occupied, representing the van der Waals surfaces for the two compounds at the GLU and MIX sites. Hydrogen atoms are not present in the crystal structure but are represented for the compound at the GLU site (from the MD simulation). **c)** RAPTA-C contacts within 2.0 Å (none). The average close contact distance is 3.8±0.3 Å.